

Preconditioned deconvolution method for high-resolution ghost imaging

ZHISHEN TONG,^{1,2} ZHENTAO LIU,¹ CHENYU HU,^{1,2} JIAN WANG,^{3,4,6} AND SHENSHENG HAN^{1,5,7}

¹Key Laboratory of Quantum Optics of CAS, Shanghai Institute of Optics and Fine Mechanics, Chinese Academy of Sciences, Shanghai 201800, China

²Center of Materials Science and Optoelectronics Engineering, University of Chinese Academy of Sciences, Beijing 100049, China

³School of Data Science, Fudan University, Shanghai 200433, China

⁴ZJLab, Shanghai Key Laboratory of Intelligent Information Processing, Shanghai 200433, China

⁵Hangzhou Institute for Advanced Study, University of Chinese Academy of Sciences, Hangzhou 310024, China

⁶e-mail: jian_wang@fudan.edu.cn

⁷e-mail: sshan@mail.shcnc.ac.cn

Received 19 January 2021; revised 21 March 2021; accepted 5 April 2021; posted 5 April 2021 (Doc. ID 420326); published 25 May 2021

Ghost imaging (GI) can nonlocally image objects by exploiting the fluctuation characteristics of light fields, where the spatial resolution is determined by the normalized second-order correlation function $g^{(2)}$. However, the spatial shift-invariant property of $g^{(2)}$ is distorted when the number of samples is limited, which hinders the deconvolution methods from improving the spatial resolution of GI. In this paper, based on prior imaging systems, we propose a preconditioned deconvolution method to improve the imaging resolution of GI by refining the mutual coherence of a sampling matrix in GI. Our theoretical analysis shows that the preconditioned deconvolution method actually extends the deconvolution technique to GI and regresses into the classical deconvolution technique for the conventional imaging system. The imaging resolution of GI after preconditioning is restricted to the detection noise. Both simulation and experimental results show that the spatial resolution of the reconstructed image is obviously enhanced by using the preconditioned deconvolution method. In the experiment, 1.4-fold resolution enhancement over Rayleigh criterion is achieved via the preconditioned deconvolution. Our results extend the deconvolution technique that is only applicable to spatial shift-invariant imaging systems to all linear imaging systems, and will promote their applications in biological imaging and remote sensing for high-resolution imaging demands. © 2021 Chinese Laser Press

<https://doi.org/10.1364/PRJ.420326>

1. INTRODUCTION

Due to diffraction of light fields, optical imaging systems act as a low-pass filter, which blocks the high-frequency information of the object [1]. A computational super-resolution imaging technique aims to recover the high-frequency information of the object outside the cutoff frequency of the optical imaging system based on the theory of the analytic continuation and non-linear operator [2]. In a conventional imaging system, by assuming the spatial shift-invariant property of the point-spread function (PSF) of the imaging system, deconvolution techniques, such as Wiener filtering [3], Richardson-Lucy algorithm [4], and Tikhonov regularization algorithm [5], have been widely exploited as super-resolution techniques for their practical feasibility [6–8].

Different from conventional imaging, ghost imaging (GI) can nonlocally achieve the image of object by conducting a high-order correlation between the detected signals without spatial resolution (referred as the object arm) and a reference light field that does not pass through the object (referred as

the reference arm) [9–12]. GI was originally developed by utilizing the quantum entangled property of two quantum entangled photons [13,14] and was later demonstrated to be realized with thermal light fields by exploiting the classical correlation property of the photons [15,16]. The key advantages of GI lie in that it decouples the detection and imaging processes and encodes the object with a fluctuation of light fields. The former makes GI more flexible than conventional imaging systems, and the latter can naturally combine compressive sensing (CS) [17,18] for image acquisition with high efficiency, and allow objects to be directly imaged in high-dimensional light-field space [19]. Owing to these advantages, GI has been widely applied in GI Lidar [20], neutron GI [21], Fourier-transform GI for X-ray [22], holographic GI [23], phase-contrast GI [24], and high-speed GI nanoscopy [25].

The diffraction-limited imaging resolution of GI is determined by the normalized second-order correlation function $g^{(2)}$ under an ensemble average [22–24,26–28], which is a counterpart to the PSF in conventional imaging systems [29]. Thus,

the idea to enhance the imaging resolution of GI by using the deconvolution technique is reported [30]. However, the spatial shift-invariant property of $g^{(2)}$ in GI only holds under the ensemble average, which is not measurable, and it will be distorted within the limited number of samples [31]. Therefore, the classical deconvolution technique fails to improve the imaging resolution of GI, especially for a small number of samples.

Inspired by the prevalent CS theory [17,18], GI via sparsity constraints (GISC) can significantly reduce the number of samples to get the desired image [12]. Specifically, the image of the object in GISC is recovered by solving an ill-posed problem:

$$\min_{\mathbf{x}} \|\mathbf{x}\|_0, \quad \text{subject to } \mathbf{y} = \mathbf{A}\mathbf{x}, \quad (1)$$

where $\mathbf{y} \in \mathbb{R}^m$ is the sampling signals measured by a detector at the object arm, $\mathbf{x} \in \mathbb{R}^n$ is the vectorized image, the sampling matrix $\mathbf{A} \in \mathbb{R}^{m \times n}$ ($m < n$) is made up of the reference arm light-field intensity, and $\|\cdot\|_0$ denotes the ℓ_0 -norm. In CS, the mutual coherence of sampling matrix is vital to affect the image recovery [32], and smaller mutual coherence generally leads to better image quality. However, the mutual coherence of the sampling matrix is directly related to the $g^{(2)}$ in GI [19], and the mutual coherence is inevitably high when the spatial structures of the object beyond the resolution limited by $g^{(2)}$ need to be resolvable. Thus, for the high-resolution imaging application of GI, its sampling matrix will be a random high-coherence matrix within a limited number of samples, which is bad for CS to recover the image.

In the last decades, preconditioned methods have been proposed to reduce the mutual coherence of the random sampling matrix and improve the reconstruction quality for sparse signals in CS [33–37]. To be specific, a matrix \mathbf{P} in the preconditioned method is multiplied to both sides of Eq. (1):

$$\min_{\mathbf{x}} \|\mathbf{x}\|_0, \quad \text{subject to } \mathbf{P}\mathbf{y} = \mathbf{P}\mathbf{A}\mathbf{x}. \quad (2)$$

By optimizing the matrix \mathbf{P} , referred to as the preconditioner in the number linear algebra [38], the mutual coherence of preconditioned sampling matrix $\mathbf{P}\mathbf{A}$ is smaller than that of sampling matrix \mathbf{A} , which contributes to better image recovery through Eq. (2). However, those existing preconditioned methods are somewhat sensitive to the unavoidable detection noise, especially for high-coherence matrices. To mitigate the influence of the detection noise, a regularized method for preconditioning has been proposed [39,40]. Although the regularized preconditioned methods have been successfully applied to practical fluorescence diffuse optical tomography, their preconditioners are designed to be square matrices for the undersampling case (i.e., $m < n$), which makes their reconstructed performances highly rely on recovery algorithms to solve Eq. (2) and be sensitive to the unknown regularization parameter as well.

In this paper, aiming at the noisy environment in practical applications, we propose a preconditioned deconvolution method to improve the imaging resolution of GI. The theoretical analysis shows that the preconditioned deconvolution method is an extension of the deconvolution technique to GI and reduces to the classical deconvolution technique for conventional imaging systems. The imaging resolution of GI

after preconditioning is restricted to the detection noise, which is consistent with the classical deconvolution technique. The effectiveness of the preconditioned deconvolution method is demonstrated on the GISC camera, which is a typical paradigm of the GI technique. Specifically, both simulations and experiments on the GISC camera system display that the imaging resolution and image quality are obviously enhanced by using the preconditioned deconvolution method. Moreover, the experimental results exhibit that 1.4-fold resolution enhancement over Rayleigh criterion of the conventional imaging system is achieved via the preconditioned deconvolution method, which could promote GI in the application of high spatial-resolution imaging scenarios. We would like to mention that the preconditioned deconvolution method utilizes prior imaging systems to overcome the diffraction limit, which is different from those super-resolution imaging methods that mainly focus on the use of sparsity priors of imaging objects in GI [25,41,42], and it can also combine prior imaging objects naturally to improve the imaging resolution furthermore.

2. METHOD

A. Preconditioning

To alleviate the influence of detection noise, the objective function of the proposed preconditioned method to solve the preconditioner \mathbf{P} is as follows:

$$\min_{\mathbf{P}} \|\mathbf{P}\mathbf{A} - \mathbf{I}\|_{\text{F}}^2 + \gamma \|\mathbf{P}\mathbf{y} - \mathbf{P}\mathbf{A}\mathbf{x}\|_2^2, \quad (3)$$

where $\|\cdot\|_{\text{F}}$ denotes the Frobenius norm, and γ is a weight factor. Different from those existing preconditioned methods, whose objective function aims to make the Gram matrix of matrix $\mathbf{P}\mathbf{A}$ approach an identity matrix, the first term of Eq. (3) is to let the matrix $\mathbf{P}\mathbf{A}$ approach an identity matrix to refine the mutual coherence of preconditioned sampling matrix $\mathbf{P}\mathbf{A}$, and the second term of Eq. (3) aims to restrict the amplification of the detection noise after preconditioning.

Let the derivative of Eq. (3) on matrix \mathbf{P} be $\mathbf{0}$, and one can find a closed-form solution of Eq. (3):

$$\mathbf{P} := \mathbf{A}^T (\mathbf{A}\mathbf{A}^T + \gamma\sigma^2\mathbf{I})^{-1}. \quad (4)$$

Specifically, the derivatives of two terms in Eq. (3) are, respectively,

$$\frac{\partial}{\partial \mathbf{P}} \|\mathbf{P}\mathbf{A} - \mathbf{I}\|_{\text{F}}^2 = 2(\mathbf{P}\mathbf{A} - \mathbf{I})\mathbf{A}^T, \quad (5)$$

and

$$\frac{\partial}{\partial \mathbf{P}} \|\mathbf{P}\mathbf{y} - \mathbf{P}\mathbf{A}\mathbf{x}\|_2^2 = 2\sigma^2\mathbf{P}, \quad (6)$$

where the detection noise \mathbf{v} (namely, $\mathbf{y} - \mathbf{A}\mathbf{x}$) is assumed as an additive white Gaussian noise (AWGN), and each element *i.i.d.* obeys the uncorrelated Gaussian distribution $\mathcal{N}(0, \sigma^2)$.

Herein we introduce two important lemmas, which will be useful for our theoretical analysis.

Lemma 1 (Woodbury Formula [43]) The following equality holds if \mathbf{A}^{-1} and \mathbf{B}^{-1} exist:

$$(\mathbf{A} + \mathbf{C}\mathbf{B}\mathbf{C}^T)^{-1} = \mathbf{A}^{-1} - \mathbf{A}^{-1}\mathbf{C}(\mathbf{B}^{-1} + \mathbf{C}^T\mathbf{A}^{-1}\mathbf{C})^{-1}\mathbf{C}^T\mathbf{A}^{-1}. \quad (7)$$

Lemma 2 (Approximations [44]) The following equality holds if \mathbf{A} is large and symmetric:

$$(\mathbf{I} + \mathbf{A})^{-1} = \mathbf{I} - \mathbf{A} + \mathbf{A}^2 - \mathbf{A}^3 + \dots \quad (8)$$

Using Eq. (4), the preconditioned sampling matrix \mathbf{PA} can be given as follows:

$$\begin{aligned} \mathbf{PA} &= \mathbf{A}^T (\mathbf{AA}^T + \gamma\sigma^2 \mathbf{I})^{-1} \mathbf{A} \\ &\stackrel{\text{Eq. (7)}}{=} \left[\frac{\mathbf{A}^T \mathbf{A}}{\gamma\sigma^2} - \left(\frac{1}{\gamma\sigma^2} \right)^2 \mathbf{A}^T \mathbf{A} \left(\mathbf{I} + \frac{\mathbf{A}^T \mathbf{A}}{\gamma\sigma^2} \right)^{-1} \mathbf{A}^T \mathbf{A} \right] \\ &\stackrel{\text{Eq. (8)}}{=} \mathbf{A}^T \mathbf{A} (\mathbf{A}^T \mathbf{A} + \gamma\sigma^2 \mathbf{I})^{-1}. \end{aligned} \quad (9)$$

In GI, the imaging resolution is characterized by the normalized second-order correlation function $g^{(2)}$, which plays the role of the PSF in the conventional imaging system [29–31]. Thus, the matrix $\mathbf{A}^T \mathbf{A}$ approaches a block circulant matrix for the large number of samples m , where the matrix $\mathbf{A}^T \mathbf{A}$ is the matrix representation of the $g^{(2)}$. Thus, $\mathbf{A}^T \mathbf{A}$ can be decomposed as [45]

$$\mathbf{A}^T \mathbf{A} = \mathbf{F}^T \mathbf{\Lambda}_1 \mathbf{F}, \quad (10)$$

where the matrices \mathbf{F} and \mathbf{F}^T are associated with the Fourier and inverse Fourier transforms (satisfying $\mathbf{FF}^T = \mathbf{F}^T \mathbf{F} = \mathbf{I}$), and $\mathbf{\Lambda}_1 = \text{diag}[\alpha_1, \dots, \alpha_n]$ is a diagonal matrix, whose diagonal elements are the Fourier coefficients of the first column of the block circulant matrix $\mathbf{A}^T \mathbf{A}$.

Substituting Eq. (10) into Eq. (9), the preconditioned sampling matrix \mathbf{PA} can be given by

$$\begin{aligned} \mathbf{PA} &= \mathbf{F}^T \mathbf{\Lambda}_1 / (\mathbf{\Lambda}_1 + \gamma\sigma^2 \mathbf{I}) \mathbf{F} \\ &= \mathbf{F}^T \text{diag} \left[\frac{\alpha_1}{\alpha_1 + \gamma\sigma^2}, \dots, \frac{\alpha_i}{\alpha_i + \gamma\sigma^2}, \dots \right] \mathbf{F} = \mathbf{F}^T \mathbf{\Lambda}_2 \mathbf{F}, \end{aligned} \quad (11)$$

where the diagonal matrix $\mathbf{\Lambda}_2 = \text{diag}[\frac{\alpha_1}{\alpha_1 + \gamma\sigma^2}, \dots, \frac{\alpha_i}{\alpha_i + \gamma\sigma^2}, \dots]$.

Equation (11) shows that the preconditioned sampling matrix \mathbf{PA} is also a block circulant matrix, and the frequency coefficient $\alpha_i / (\alpha_i + \gamma\sigma^2)$ of the matrix \mathbf{PA} approaches one as the detection noise reaches 0, which implies that the improvement of spatial resolution of matrix \mathbf{PA} is limited to the detection noise. One can interpret from Eq. (11) that directly multiplying the preconditioner \mathbf{P} to the sampling signals \mathbf{y} formally is the same as the deconvolution technique in the classical convolution model [46,47]. The difference is that the sampling matrix \mathbf{A} in GI is a random matrix, whereas that in the classical convolution model is a block circulant matrix. Specifically, for the spatial shift-invariant imaging system, which can be described as a classical convolution model, its sampling matrix \mathbf{A} is a block circulant matrix. Thus, \mathbf{A} can be similarly decomposed as follows:

$$\mathbf{A} = \mathbf{F}^T \mathbf{\Lambda}'_1 \mathbf{F}, \quad (12)$$

where $\mathbf{\Lambda}'_1 = \text{diag}[\alpha'_1, \dots, \alpha'_n]$ is a diagonal matrix whose diagonal elements are the Fourier coefficients of the PSF of the conventional imaging system. Correspondingly, Eq. (9) becomes

$$\begin{aligned} \mathbf{PA} &= \mathbf{F}^T \mathbf{\Lambda}'_1 / (\mathbf{\Lambda}'_1 + \gamma\sigma^2 \mathbf{I}) \mathbf{F} \\ &= \mathbf{F}^T \text{diag} \left[\frac{\alpha'_1}{\alpha'_1 + \gamma\sigma^2}, \dots, \frac{\alpha'_i}{\alpha'_i + \gamma\sigma^2}, \dots \right] \mathbf{F}, \end{aligned} \quad (13)$$

which regresses into the classical deconvolution technique [47].

We would like to mention that the preconditioned method for the noiseless case, i.e., $\sigma^2 = 0$, has the same form as the pseudo-inverse GI method [48,49]. Unfortunately, the performances of the pseudo-inverse GI method are sensitive to the detection noise, which hampers their practical applications.

B. GISC Camera

As a typical paradigm of the GI technique, the GISC camera can simultaneously achieve an object's high-dimensional (e.g., spatial, spectral, polarized) information with one snapshot by encoding the high-dimensional information of light fields irradiating from the object into speckle patterns on a detectable two-dimensional (2D) plane [27]. Figure 1 shows the setup of the GISC camera, which applies a spatial random phase modulator (SRPM) after the image plane of conventional imaging systems, such as a microscope and telescope, to modulate the light field irradiating from the object into the speckle field that is detected by detector 2. In the GISC camera, each pixel of detector 2 acts like a bucket detector or single-pixel detector and contains information from all pixels in the image, which is the main feature of the object beam in GI. Correspondingly, the image of the GISC camera can be reconstructed by conducting a high-order correlation between the detected signals and the predetermined reference light-field patterns under the spatial ensemble average. For GI calculating the ensemble average in the time domain, a bucket detector or single-pixel detector is adopted to measure the modulated signal irradiating from the objects, where the fluctuation of the illuminating light fields needs to be changed per measurement. Because a large number of measurements are needed to obtain the desired image, the GI ensemble averaged in the time domain generally demands long image acquisition time. By converting the calculation of the ensemble average in the time domain to the spatial domain, the GISC camera achieves the image in one snapshot, which overcomes the shortage of long image

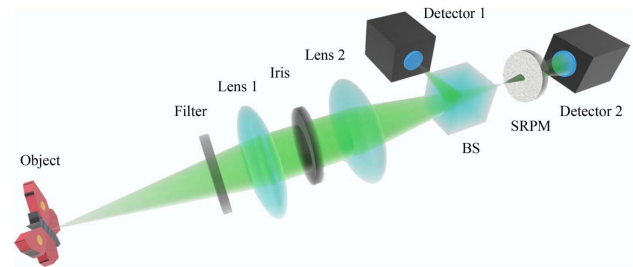


Fig. 1. Experimental setup of the GISC camera. A conventional imaging system, which consists of the filter, lens 1 with focus length f_1 , lens 2 with focus length f_2 , and iris with diameter D , projects the object into its image plane. A spatial random phase modulator (SRPM) is set before detector 2 to modulate the image of the object into a speckle image, which is recorded on detector 2. For comparison, a ground-truth image of the object is recorded on detector 1 through the conventional imaging system with a large aperture diameter of the iris by another optical path via a beam splitter (BS).

acquisition time and makes it possible to observe high-speed dynamic processes. Although the GISC camera needs a certain detection signal-to-noise ratio (SNR) to guarantee image recovery, its image acquisition is fast because only one snapshot is required to achieve the image.

In this paper, we focus on improving the spatial resolution of the GISC camera. By calculating the second-order correlation function between the intensity fluctuations at the predetermined reference arm and the object arm, the spatial image of object can be achieved [27]:

$$\begin{aligned} \Delta G^{(2,2)}(\mathbf{x}_r) &= \langle \Delta I_r(\mathbf{x}_t) \Delta I_r(\mathbf{x}_t; \mathbf{x}_r) \rangle_{\mathbf{x}_t} \\ &\propto \int T(\mathbf{x}') g^{(2)}(\mathbf{x}_r, \mathbf{x}') d\mathbf{x}', \end{aligned} \quad (14)$$

where $T(\mathbf{x}_r)$ represents the spatial image of object, $I_r(\mathbf{x}_t)$ is the speckle image, and $I_r(\mathbf{x}_t; \mathbf{x}_r)$ denotes the speckle pattern of the GISC camera corresponding to one monochrome point light source at the position \mathbf{x}_r . \mathbf{x}_t and \mathbf{x}_r are 2D vectors on the object plane and the detection plane of the GISC camera, respectively, and $\langle \cdot \rangle_{\mathbf{x}_t}$ means the spatial ensemble average over the coordinate \mathbf{x}_t . The normalized second-order correlation function $g^{(2)}(\mathbf{x}_r, \mathbf{x}_r')$ describes the spatial resolution of the GISC camera.

The spatial image of object can be also retrieved by solving an inverse problem:

$$\min_{\mathbf{x}} \|\mathbf{x}\|_0 \quad \text{subject to } \mathbf{y} - \bar{\mathbf{y}} = (\mathbf{A} - \bar{\mathbf{A}})\mathbf{x}, \quad (15)$$

where the sampling matrix \mathbf{A} is made up of speckle patterns $I_r(\mathbf{x}_t; \mathbf{x}_r)$, the sampling signal \mathbf{y} consists of the speckle image $I_r(\mathbf{x}_t)$, \mathbf{x} represents the spatial image, and $\bar{\cdot}$ denotes an average operator to calculate the mean value of the columns of matrix \mathbf{A} and vector \mathbf{y} . For notational simplicity, denote $\Phi = \mathbf{A} - \bar{\mathbf{A}}$. As mentioned in Ref. [19], the mutual coherence of matrix Φ is equal to the maximum value of $g^{(2)}(\mathbf{x}_r, \mathbf{x}_r')$, which represents the correlation of speckle patterns corresponding to the two nearest points on the object plane. Thus, for the high-resolution imaging application, the mutual coherence of matrix Φ is naturally large, which is not good for high-resolution image recovery.

3. SIMULATIONS AND EXPERIMENTS

A. Experimental Setup and Construction of Sampling Matrix

Figure 1 shows the experimental setup of the GISC camera. To be specific, an object is projected on the image plane through the conventional imaging system, which is made up of a filter (FL 532-3, Thorlabs), lens 1 (AF70-300 mm, TAmRon) with focus length 300 mm, lens 2 (AF70-300 mm, TAmRon) with focus length 300 mm, and an iris with diameter 25 mm. The image of the object is modulated into a speckle image by an SRPM (DGUV 10-1500, Thorlabs), and is directly recorded on detector 2 (iKon-M, Andor, pixel size of 13 μm). The SRPM is placed after the image plane of the conventional imaging system with distance 9.7 mm, and is set before detector 2 with distance 40 mm. For comparative purposes, the ground-truth image of the object through the conventional imaging system with a large aperture diameter is recorded on detector 1 (Stingray F-504B, Allied Vision) at another optical path split by a 10/90 (R:T) beam splitter (BS043, Thorlabs). The GISC

camera system was built on an indoor optical platform, where the objects were illuminated by a white light source through the arc lamp (Arc lamp 66902, Newport).

Before imaging, we need to calibrate the GISC camera for constructing the sampling matrix \mathbf{A} . In the calibration process, a fiber (core diameter 16 μm) coupling with incident light ($\lambda = 532 \text{ nm}$) acts as a point source, which is mounted on an electric translation stage. A series of speckle images are generated by shifting the point source at a step size of 3 μm in the whole 400 $\mu\text{m} \times 400 \mu\text{m}$ field of view (FoV). Then, the sampling matrix \mathbf{A} is built in the following way, namely, each column of the sampling matrix consists of speckle images by reshaping a 2D speckle image into a column vector. In the imaging process, we just replace the point source with the imaging object and record the corresponding speckle image on detector 2 with one snapshot, which makes up the sampling signal \mathbf{y} in the same processing manner as that in the calibration process.

B. Simulation Results

In order to validate the proposed preconditioned deconvolution method for improving the reconstruction performance of the GISC camera, we carry out numerical simulations. In the simulation, we adopt the real speckle patterns obtained in the calibration process, and the sampling signal \mathbf{y} is generated via $\mathbf{y} = \mathbf{A}\mathbf{x} + \mathbf{v}$. The images of object \mathbf{x} are constructed as shown in Fig. 2. Herein the detection noise \mathbf{v} is assumed as an AWGN, and the noise level is measured by the detection SNR, which is defined as $\text{SNR} = 10 \log_{10}(\bar{y}/\sigma^2)$ (dB), where \bar{y} is the mean values of the sampling signal \mathbf{y} , and σ^2 is the variance of the distribution of AWGN.

The first simulation aims to show how effective the proposed preconditioned deconvolution method is in reducing the mutual coherence of sampling matrices. To this end, we compare the mutual coherence of the sampling matrix before and after the proposed preconditioned deconvolution method, as well as the normalized mutual correlation function. As observed in Figs. 2(a) and 2(b), the mutual coherence of preconditioned matrix $\mathbf{P}\Phi$ is uniformly smaller than that of original matrix Φ among the tested sampling rates $\eta = m/n$, where m is the number of samples and n is the number of pixels of the vectorized image \mathbf{x} , and the width of the normalized mutual correlation curve of preconditioned matrix $\mathbf{P}\Phi$ is sharper than that of original matrix Φ , which implies that the spatial resolution could be enhanced after preconditioning. One can see that the mutual coherence of Φ approaches a lower bound as the sampling rate increases, which is fundamentally restricted to the resolution limit by the $g^{(2)}$ in GI. Overall, the effectiveness of the proposed preconditioned deconvolution method to refine the sampling matrix is clearly demonstrated in the simulation.

Next, we empirically compare the image reconstruction of the preconditioned deconvolution method with other approaches. For comparative purposes, the representative approaches including differential GI (DGI) [50], two-step iterative shrinkage/thresholding (TwIST) for sparse signal recovery [51], the proposed preconditioned GI (PreGI, namely, the proposed preconditioner \mathbf{P} directly multiplies the sampling signal \mathbf{y}), and the proposed preconditioned deconvolution method plus TwIST [PreTwIST, namely, solving Eq. (2) with

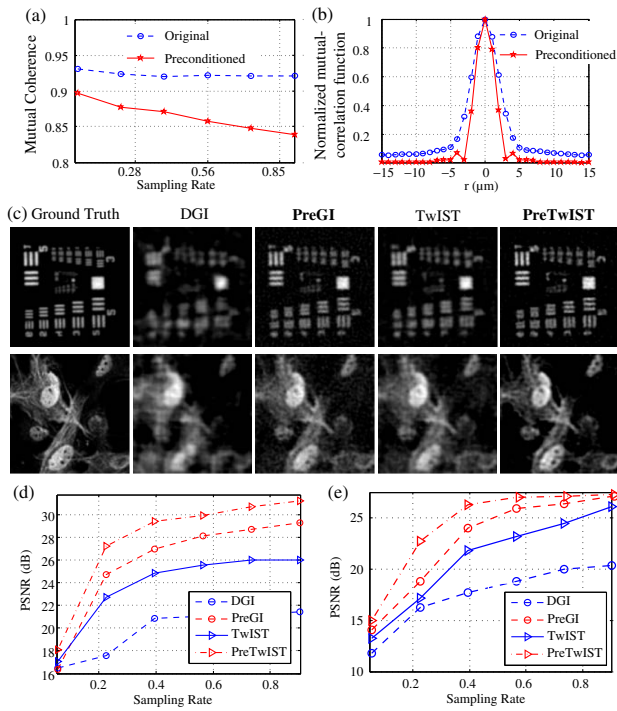


Fig. 2. Mutual coherence comparison and recovery performance comparison among DGI, PreGI, TwIST, and PreTwIST algorithms at different sampling rates. (a) Mutual coherence as a function of sampling rate; (b) normalized mutual correlation function of original matrix Φ and preconditioned matrix $P\Phi$; (c) recovery results of DGI, PreGI, TwIST, and PreTwIST algorithms at the sampling rate 0.4 under the detection signal-to-noise ratio (SNR) 25 dB; (d), (e) recovery comparison for the resolution target and cell image with a size of 133×133 pixels through the PSNR between DGI, PreGI, TwIST, and PreTwIST at different sampling rates.

the TwIST from the preconditioned sampling signals $P\mathbf{y}$] algorithm are adopted. Figure 2(c) represents the imaging results of the resolution target and cell image by DGI, PreGI, TwIST, and PreTwIST algorithms under the detection SNR 25 dB at a sampling rate of 0.4, and Figs. 2(d) and 2(e) exhibit the comparison of image quality under different sampling rates by adopting the quantitative evaluation metric: peak SNR (PSNR) [52]. Clearly, the image quality of the GISC camera is greatly improved after the proposed preconditioned operator.

To investigate the improvement of image quality by the preconditioned deconvolution method in the noisy environment, we perform simulations and compare the recovery performance by the abovementioned algorithms under different noisy levels. In the simulation, the detection SNRs are set from 15 dB to 45 dB with increasing step 5 dB, and the sampling rate is $\eta = 0.4$. Figure 3(a) presents the normalized mutual correlation function of the preconditioned matrix $P\Phi$ at different detection SNRs. One can observe that the width of the mutual correlation curve gets small when the detection SNR increases, which matches our theoretical analysis results well. Moreover, both Figs. 3(b)–3(d) show that the image quality of the GISC camera is indeed improved by the proposed preconditioned deconvolution method among the tested detection SNRs, and the improvement gets big as the detection SNR increases. Overall,

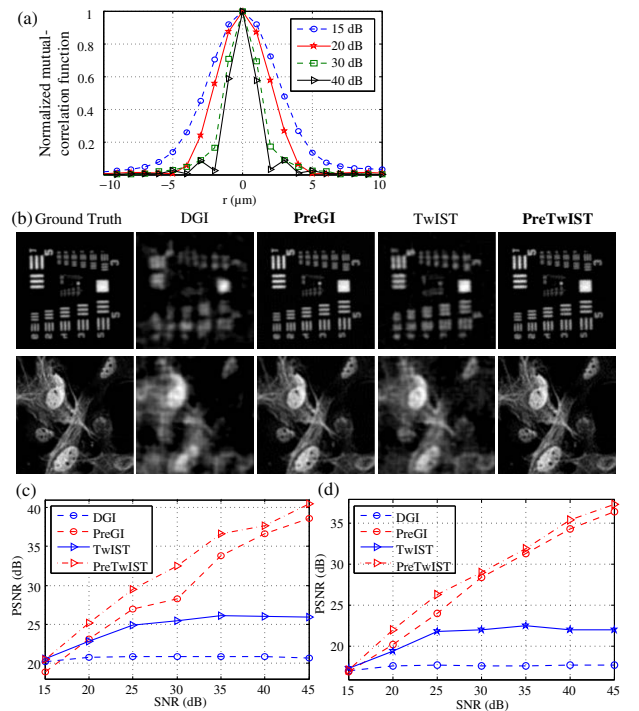


Fig. 3. Simulated recovery results by DGI, PreGI, TwIST, and PreTwIST algorithms under different detection SNRs. (a) Normalized mutual correlation function of preconditioned matrix $P\Phi$ under different detection SNRs; (b) reconstructed results of DGI, PreGI, TwIST, and PreTwIST algorithms at the sampling rate 0.4 under the detection SNR 40 dB; (c), (d) recovery comparison for the resolution target and cell image with a size of 133×133 pixels through the PSNR between DGI, PreGI, TwIST, and PreTwIST under different detection SNRs.

the simulation results demonstrate the effectiveness of the preconditioned deconvolution method in refining the sampling matrix and improving the image quality of the GISC camera.

C. Experimental Results

In this section, we apply the proposed preconditioned deconvolution method to dealing with the experimental data of the GISC camera. In the experiment, we image five objects, including the transmission objects and reflective objects. Figure 4 shows the imaging results of different objects by the DGI, PreGI, TwIST, and PreTwIST algorithms. The left column in Fig. 4 represents the ground-truth images of objects, which are achieved through a conventional imaging system as shown in Fig. 1 with an aperture diameter 25 mm of the iris. It can be observed that the PreTwIST algorithm achieves the best results compared with the other approaches, especially in clearing the background noise of the image. Moreover, as shown in Fig. 4(d), the preconditioned deconvolution method can obviously improve the spatial resolution of the image compared with the DGI method.

We also test the recovery performance by using the preconditioned deconvolution method under different sampling rates and different detection SNRs. In the experiment, the detection noise is mainly limited to the shot noise, and the detection SNR is measured by $\text{SNR} = 10 \log_{10} \sqrt{N}$ (dB), where N denotes

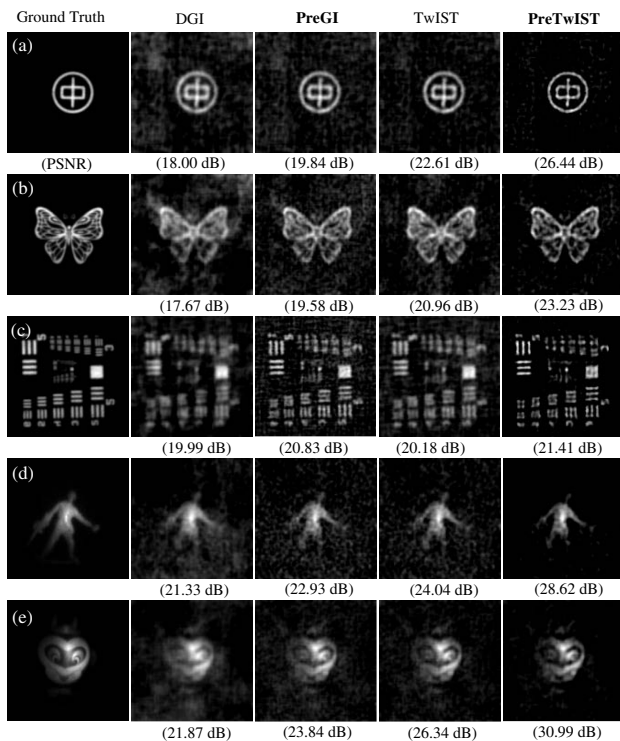


Fig. 4. Experimental results of DGI, PreGI, TwIST, and PreTwIST algorithms for five different objects with a size of 133×133 pixels, where the (a)–(c) represent the transmission objects and (d), (e) denote the reflective objects. The sampling rate for objects (a), (b) is 0.23, and for objects (c)–(e) is 0.45. The detection SNRs for objects (a)–(e) are, respectively, 24.8 dB, 24.7 dB, 24.8 dB, 20.0 dB, and 23.2 dB.

the average photon number which can be estimated from the number of electronics recorded on detector 2. Figure 5 shows the PSNR of the reconstructed image of the transmission object resolution target under different sampling rates and different detection SNRs. It can be observed that the reconstruction quality is uniformly improved after the preconditioned deconvolution method among the tested sampling rates and detection SNRs.

D. Extended to Super-Resolution Imaging

In this section, we extend the preconditioned deconvolution method to super-resolution imaging. Following the requirement of Ref. [19], where the spatial resolution of the modu-

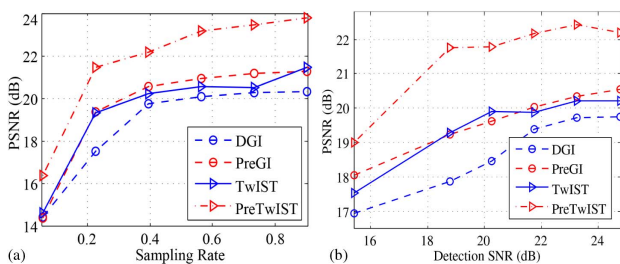


Fig. 5. Experimental comparison of the PSNR results of the resolution target with a size of 133×133 pixels by using DGI, PreGI, TwIST, and PreTwIST algorithms under (a) different sampling rates and (b) different detection SNRs.

lation module is much higher than that of the conventional imaging module in the GISC camera, we adjust the parameters of the GISC camera to make the spatial resolution of the GISC camera approach the Rayleigh limit of the conventional imaging system. To be specific, the diameter of aperture is set as 10 mm, the distance between the first image plane and the

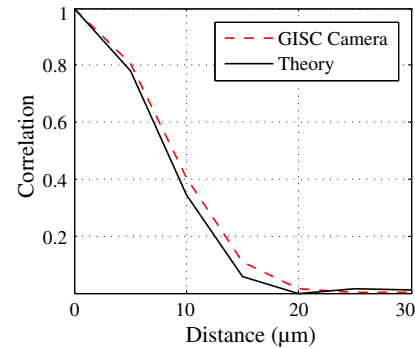


Fig. 6. Comparison of the normalized mutual correlation function of the GISC camera and the theoretical result. The theoretical result is the Rayleigh criterion with incident wavelength 532 nm.

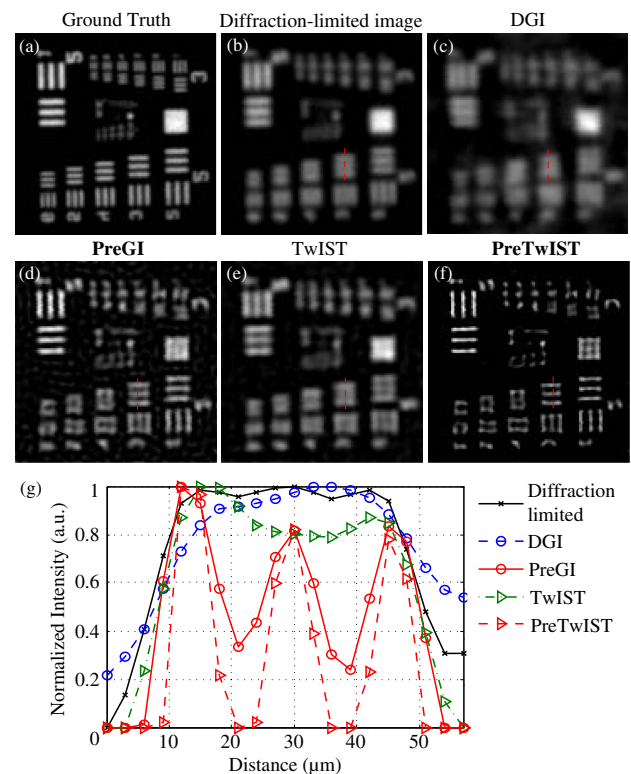


Fig. 7. Experimental results of resolution target with a size of 120×120 pixels for super-resolution imaging. (a) Ground-truth image of the object is recorded by a conventional imaging system with a large aperture diameter of 25 mm; (b) diffraction-limited image of the object via the conventional imaging system with a small aperture diameter of 10 mm; recovery results by (c) DGI, (d) PreGI, (e) TwIST, and (f) PreTwIST; (g) comparison of resolution, intensity profiles extracted from the cross-section black lines in subfigures (b)–(f).

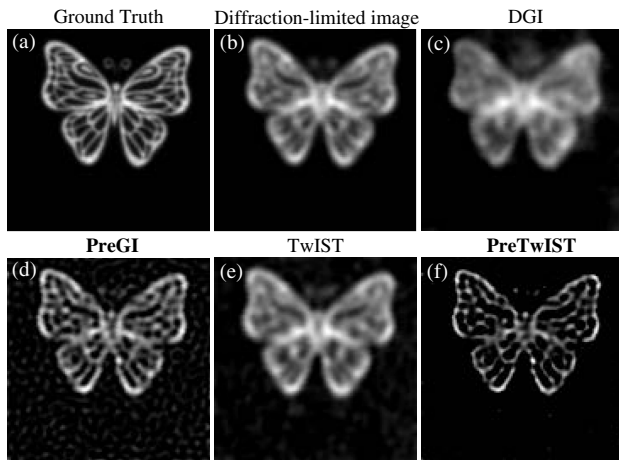


Fig. 8. Experimental results of a butterfly target with a size of 120×120 pixels for super-resolution imaging. (a) Ground-truth image of the object is recorded by a conventional imaging system with a large aperture diameter of 25 mm; (b) diffraction-limited image of the object via the conventional imaging system with a small aperture diameter of 10 mm; recovery results by (c) DGI, (d) PreGI, (e) TwIST, and (f) PreTwIST.

SRPM is changed into 2.7 mm, and the distance between the SRPM and detector 2 is 15 mm. Figure 6 reveals that the normalized mutual correlation function of the GISC camera approaches the theoretical Rayleigh limit of the conventional imaging system at an incident wavelength of 532 nm. The Rayleigh limit of the conventional imaging system in its image plane before the SRPM of the GISC camera is about $19.5 \mu\text{m}$.

Figure 7 shows reconstructed images of the resolution target by the aforementioned four algorithms. Compared with the imaging results of DGI and TwIST algorithms, the proposed PreGI algorithm and PreTwIST algorithm achieve much higher imaging resolution. Particularly, the resolution below $13.8 \mu\text{m}$ can be obviously recognized by PreGI and PreTwIST algorithms. Considering the Rayleigh criterion $19.5 \mu\text{m}$, both the imaging results of PreGI and PreTwIST algorithms achieve a 1.4-fold resolution enhancement over the Rayleigh criterion in this experiment. Moreover, as shown in Figs. 7(d), 7(f), and 7(g), the imaging result of the PreTwIST algorithm has a much clearer background and higher resolution than that of PreGI. Also, a much complicated object butterfly is tested in the experiment. Figure 8 presents images of a butterfly by the aforementioned algorithms. It shows that the PreGI and PreTwIST algorithms achieve higher imaging resolution than DGI and TwIST algorithms. Overall, the proposed preconditioned deconvolution method exhibits competitive advantages in super-resolution imaging.

4. DISCUSSION AND CONCLUSION

For conventional imaging systems, by exploiting the sparsity-imposing priors of imaging objects and the prior information of imaging systems with the assumption of the spatial shift-invariant property of the PSF, super-resolution imaging methods via sparsity constraints, which are based on the sparsity priors of imaging objects, and the deconvolution techniques that

use the prior of the PSF of imaging systems have been widely studied [7,8,53–55]. However, existing GI techniques to improve the imaging resolution mainly focus on the use of sparsity priors of imaging objects in reconstruction [25,41,42], and rarely take prior imaging systems into account, because the spatial shift-invariant property of $g^{(2)}$ is distorted within the limited number of samples. In this work, with the proposed preconditioned deconvolution method based on prior GI systems, the classical deconvolution method is extended to GI systems for improving the imaging resolution. The simulation and experimental results demonstrate that both the methods using the sparsity prior of imaging objects and the proposed preconditioned deconvolution method applying the prior of imaging systems can effectively improve the imaging resolution of GI. Moreover, the combination of the sparsity prior of imaging objects and the prior of imaging systems achieves the best performance in the improvement of GI's imaging resolution.

For linear imaging systems, where the imaging model of those systems can be expressed as $\mathbf{y} = \mathbf{A}\mathbf{x}$ and the sampling matrix \mathbf{A} can be structured matrices or random matrices, such as the fluorescent microscopy, telescope, aperture coding imaging system, computational GI, and single-pixel imaging, the preconditioned deconvolution method offers new possibilities to improve the imaging performance of all those systems. Although the computational cost of the inverse operator for a large-scale matrix in the proposed preconditioned deconvolution method is inevitably high, the preconditioner \mathbf{P} can be obtained in advance through highly effective computation servers. Moreover, the computational cost for the inverse operator is expected to decrease by dividing a large-scale matrix into several small-scale matrices and further solving a partitioned matrix [56].

Existing preconditioned methods achieving the preconditioner are to make the Gram matrix of the preconditioned sampling matrix \mathbf{PA} approach an identity matrix [33–37,39,40]. Those Gram-matrix methods are mathematically strict because the mutual coherence of a preconditioned sampling matrix equals the largest non-diagonal element of its Gram matrix. However, the objective function of those Gram-matrix methods is a non-convex function, and the optimal preconditioner \mathbf{P} is obtained in an iterative fashion. Different from those Gram-matrix preconditioned methods, the proposed preconditioned method is to let the preconditioned sampling matrix \mathbf{PA} directly approach an identity matrix. Although it is an indirect way in mathematics to make its Gram matrix reach the identity matrix, thereby reducing the mutual coherence, the objective function of the proposed method is a convex function, which exists within the optimal closed-form solution. Moreover, the idea to make the preconditioned sampling matrix \mathbf{PA} close to the identity matrix can reduce the interference between the adjacent pixels of image \mathbf{x} that pass through the imaginary system corresponding to the preconditioned sampling matrix \mathbf{PA} . Therefore, combined with the noise constraint, the objective function of the proposed preconditioned method has clear physical interpretations.

In conclusion, based on prior imaging systems, we presented a preconditioned deconvolution method to improve the spatial resolution of GI by refining the mutual coherence of the

sampling matrix corresponding to the imaging system. Our theoretical analysis shows that the spatial resolution of GI after preconditioning is still restricted to the detection noise, and the preconditioning method actually is an extension of the classical deconvolution technique of GI. As a typical paradigm of the GI technique, the GISC camera was implemented to validate the effectiveness of the proposed preconditioned deconvolution method. Both simulation and experimental results demonstrate that the spatial resolution and image quality of the GISC camera are greatly enhanced by using the preconditioned deconvolution method. Owing to the high efficiency of information acquisition, the GISC camera has been successfully applied to fluorescent microscopy [25] and remote sensing [27,57]. Therefore, in conjunction with the GISC camera, the preconditioned deconvolution method is expected to promote the applications of GI for high spatial and temporal resolution imaging scenarios, such as live cells imaging and remote sensing.

Funding. National Key Research and Development Program of China (2017YFB0503303); National Natural Science Foundation of China (61991454, 11627811, 61971146); Shanghai Municipal Science and Technology Major Project (2018SHZDZX01); Open Project of Chinese Academy of Sciences.

Disclosures. The authors declare no conflicts of interest.

REFERENCES

1. E. Abbe, *Beitrag zur Theorie des Mikroskops und der mikroskopischen Wahrnehmung* (Archiv für Mikroskopische Anatomie, 1873), pp. 413–468.
2. S. Chaudhuri, *Super-resolution Imaging* (Springer, 2001), Vol. 632.
3. J. W. Tukey, “The extrapolation, interpolation and smoothing of stationary time series with engineering applications,” *J. Am. Stat. Assoc.* **47**, 319–321 (1952).
4. L. B. Lucy, “An iterative technique for the rectification of observed distributions,” *Astron. J.* **79**, 745–754 (1974).
5. A. N. Tikhonov, “On the solution of ill-posed problems and the method of regularization,” in *Doklady Akademii Nauk* (Russian Academy of Sciences, 1963), Vol. 151, pp. 501–504.
6. J.-L. Starck, E. Pantin, and F. Murtagh, “Deconvolution in astronomy: a review,” *Publ. Astron. Soc. Pac.* **114**, 1051–1069 (2002).
7. P. Sarder and A. Nehorai, “Deconvolution methods for 3-D fluorescence microscopy images,” *IEEE Signal Process. Mag.* **23**, 32–45 (2006).
8. H.-X. He, X.-S. Xie, Y.-K. Liu, H.-W. Liang, and J.-Y. Zhou, “Exploiting the point spread function for optical imaging through a scattering medium based on deconvolution method,” *J. Innov. Opt. Health Sci.* **12**, 1930005 (2019).
9. J. H. Shapiro and R. W. Boyd, “The physics of ghost imaging,” *Quantum Inf. Process.* **11**, 949–993 (2012).
10. T. Shirai, “Modern aspects of intensity interferometry with classical light,” *Prog. Opt.* **62**, 1–72 (2017).
11. P.-A. Moreau, E. Toninelli, T. Gregory, and M. J. Padgett, “Ghost imaging using optical correlations,” *Laser Photon. Rev.* **12**, 1700143 (2018).
12. S. Han, H. Yu, X. Shen, H. Liu, W. Gong, and Z. Liu, “A review of ghost imaging via sparsity constraints,” *Appl. Sci.* **8**, 1379 (2018).
13. T. B. Pittman, Y. Shih, D. Strekalov, and A. V. Sergienko, “Optical imaging by means of two-photon quantum entanglement,” *Phys. Rev. A* **52**, R3429–R3432 (1995).
14. D. Strekalov, A. Sergienko, D. Klyshko, and Y. Shih, “Observation of two-photon ‘ghost’ interference and diffraction,” *Phys. Rev. Lett.* **74**, 3600–3603 (1995).
15. A. Gatti, E. Brambilla, M. Bache, and L. A. Lugiato, “Ghost imaging with thermal light: comparing entanglement and classical correlation,” *Phys. Rev. Lett.* **93**, 093602 (2004).
16. J. Cheng and S. Han, “Incoherent coincidence imaging and its applicability in X-ray diffraction,” *Phys. Rev. Lett.* **92**, 093903 (2004).
17. E. J. Candes and T. Tao, “Decoding by linear programming,” *IEEE Trans. Inf. Theory* **51**, 4203–4215 (2005).
18. D. L. Donoho, “Compressed sensing,” *IEEE Trans. Inf. Theory* **52**, 1289–1306 (2006).
19. Z. Tong, Z. Liu, J. Wang, X. Shen, and S. Han, “Breaking Rayleigh’s criterion via discernibility in high-dimensional light-field space with snapshot ghost imaging,” arXiv:2004.00135 (2020).
20. C. Zhao, W. Gong, M. Chen, E. Li, H. Wang, W. Xu, and S. Han, “Ghost imaging lidar via sparsity constraints,” *Appl. Phys. Lett.* **101**, 141123 (2012).
21. Y.-H. He, Y.-Y. Huang, Z.-R. Zeng, Y.-F. Li, J.-H. Tan, L.-M. Chen, L.-A. Wu, M.-F. Li, B.-G. Quan, S.-L. Wang, and T.-J. Liang, “Single-pixel imaging with neutrons,” *Sci. Bull.* **66**, 133–138 (2021).
22. H. Yu, R. Lu, S. Han, H. Xie, G. Du, T. Xiao, and D. Zhu, “Fourier-transform ghost imaging with hard X rays,” *Phys. Rev. Lett.* **117**, 113901 (2016).
23. X.-B. Song, D.-Q. Xu, H.-B. Wang, J. Xiong, X. Zhang, D.-Z. Cao, and K. Wang, “Experimental observation of one-dimensional quantum holographic imaging,” *Appl. Phys. Lett.* **103**, 131111 (2013).
24. D.-J. Zhang, Q. Tang, T.-F. Wu, H.-C. Qiu, D.-Q. Xu, H.-G. Li, H.-B. Wang, J. Xiong, and K. Wang, “Lensless ghost imaging of a phase object with pseudo-thermal light,” *Appl. Phys. Lett.* **104**, 121113 (2014).
25. W. Li, Z. Tong, K. Xiao, Z. Liu, Q. Gao, J. Sun, S. Liu, S. Han, and Z. Wang, “Single-frame wide-field nanoscopy based on ghost imaging via sparsity constraints,” *Optica* **6**, 1515–1523 (2019).
26. W. Gong, C. Zhao, H. Yu, M. Chen, W. Xu, and S. Han, “Three-dimensional ghost imaging lidar via sparsity constraint,” *Sci. Rep.* **6**, 26133 (2016).
27. Z. Liu, S. Tan, J. Wu, E. Li, X. Shen, and S. Han, “Spectral camera based on ghost imaging via sparsity constraints,” *Sci. Rep.* **6**, 25718 (2016).
28. X.-H. Chen, F.-H. Kong, Q. Fu, S.-Y. Meng, and L.-A. Wu, “Sub-Rayleigh resolution ghost imaging by spatial low-pass filtering,” *Opt. Lett.* **42**, 5290–5293 (2017).
29. Y. Gao, Y. Bai, and X. Fu, “Point-spread function in ghost imaging system with thermal light,” *Opt. Express* **24**, 25856–25866 (2016).
30. Z. Chen, J. Shi, Y. Li, Q. Li, and G. Zeng, “Super-resolution thermal ghost imaging based on deconvolution,” *Eur. Phys. J. Appl. Phys.* **67**, 10501 (2014).
31. Z. Li, Q. Zhao, and W. Gong, “Distorted point spread function and image reconstruction for ghost imaging,” *Opt. Lasers Eng.* **139**, 106486 (2021).
32. E. J. Candes, “The restricted isometry property and its implications for compressed sensing,” *C. R. Math.* **346**, 589–592 (2008).
33. M. Elad, “Optimized projections for compressed sensing,” *IEEE Trans. Signal Process.* **55**, 5695–5702 (2007).
34. J. M. Duarte-Carvajalino and G. Sapiro, “Learning to sense sparse signals: simultaneous sensing matrix and sparsifying dictionary optimization,” *IEEE Trans. Image Process.* **18**, 1395–1408 (2009).
35. E. Tsiligianis, L. P. Kondi, and A. K. Katsaggelos, “Preconditioning for underdetermined linear systems with sparse solutions,” *IEEE Signal Process. Lett.* **22**, 1239–1243 (2015).
36. X. Liao, H. Li, and L. Carin, “Generalized alternating projection for weighted- $2,1$ minimization with applications to model-based compressive sensing,” *SIAM J. Imaging Sci.* **7**, 797–823 (2014).
37. X. Yuan, “Adaptive step-size iterative algorithm for sparse signal recovery,” *Signal Process.* **152**, 273–285 (2018).
38. M. Benzi, “Preconditioning techniques for large linear systems: a survey,” *J. Comput. Phys.* **182**, 418–477 (2002).
39. R. Yao, Q. Pian, and X. Intes, “Wide-field fluorescence molecular tomography with compressive sensing based preconditioning,” *Biomed. Opt. Express* **6**, 4887–4898 (2015).
40. A. Jin, B. Yazici, A. Ale, and V. Ntzichristos, “Preconditioning of the fluorescence diffuse optical tomography sensing matrix based on compressive sensing,” *Opt. Lett.* **37**, 4326–4328 (2012).

41. W. Gong and S. Han, "Experimental investigation of the quality of lensless super-resolution ghost imaging via sparsity constraints," *Phys. Lett. A* **376**, 1519–1522 (2012).
42. W. Gong and S. Han, "High-resolution far-field ghost imaging via sparsity constraint," *Sci. Rep.* **5**, 9280 (2015).
43. W. W. Hager, "Updating the inverse of a matrix," *SIAM Rev.* **31**, 221–239 (1989).
44. D. Colquhoun and A. G. Hawkes, "A Q-matrix cookbook," in *Single-channel Recording* (Springer, 1995), pp. 589–633.
45. N. Zhao, Q. Wei, A. Basarab, N. Dobigeon, D. Kouamé, and J.-Y. Tourneret, "Fast single image super-resolution using a new analytical solution for l_2 - l_2 problems," *IEEE Trans. Image Process.* **25**, 3683–3697 (2016).
46. M. D. Robinson, C. A. Toth, J. Y. Lo, and S. Farsiu, "Efficient Fourier-wavelet super-resolution," *IEEE Trans. Image Process.* **19**, 2669–2681 (2010).
47. R. Neelamani, H. Choi, and R. Baraniuk, "Forward: Fourier-wavelet regularized deconvolution for ill-conditioned systems," *IEEE Trans. Signal Process.* **52**, 418–433 (2004).
48. C. Zhang, S. Guo, J. Cao, J. Guan, and F. Gao, "Object reconstitution using pseudo-inverse for ghost imaging," *Opt. Express* **22**, 30063–30073 (2014).
49. W. Gong, "High-resolution pseudo-inverse ghost imaging," *Photon. Res.* **3**, 234–237 (2015).
50. F. Ferri, D. Magatti, L. Lugiato, and A. Gatti, "Differential ghost imaging," *Phys. Rev. Lett.* **104**, 253603 (2010).
51. J. M. Bioucas-Dias and M. A. Figueiredo, "A new twist: two-step iterative shrinkage/thresholding algorithms for image restoration," *IEEE Trans. Image Process.* **16**, 2992–3004 (2007).
52. Z. Wang, A. C. Bovik, H. R. Sheikh, and E. P. Simoncelli, "Image quality assessment: from error visibility to structural similarity," *IEEE Trans. Image Process.* **13**, 600–612 (2004).
53. S. Gazit, A. Szameit, Y. C. Eldar, and M. Segev, "Super-resolution and reconstruction of sparse sub-wavelength images," *Opt. Express* **17**, 23920–23946 (2009).
54. L. Zhu, W. Zhang, D. Elnatan, and B. Huang, "Faster storm using compressed sensing," *Nat. Methods* **9**, 721–723 (2012).
55. E. J. Candès and C. Fernandez-Granda, "Towards a mathematical theory of super-resolution," *Commun. Pure Appl. Math.* **67**, 906–956 (2014).
56. C.-H. Hung and T. L. Markham, "The Moore-Penrose inverse of a partitioned matrix $M = \begin{pmatrix} A & D \\ B & C \end{pmatrix}$," *Linear Algebra Appl.* **11**, 73–86 (1975).
57. J. Wu, E. Li, X. Shen, S. Yao, Z. Tong, C. Hu, Z. Liu, S. Liu, S. Tan, and S. Han, "Experimental results of the balloon-borne spectral camera based on ghost imaging via sparsity constraints," *IEEE Access* **6**, 68740–68748 (2018).